Hydrodynamic simulation of subpicosecond laser interaction with solid-density matter

K. Eidmann, J. Meyer-ter-Vehn, and T. Schlegel

Max-Planck-Institut für Quantenoptik, Hans Kopfermannstrasse 1, D-85748 Garching, Germany

S. Hüller

Centre de Physique Théorique, Ecole Polytechnique, F-91128, France

(Received 23 December 1999)

The interaction of ultrashort subpicosecond laser pulses with initially cold and solid matter is investigated in a wide intensity range (10^{11} to 10^{17} W/cm^2) by means of the hydrodynamic code MULTI-FS, which is an extension of the long pulse version of MULTI [R. Ramis, R. Schmalz, and J. Meyer-ter-Vehn, Comput. Phys. Commun. **49**, 475 (1988)]. Essential modifications for the treatment of ultrashort pulses are the solution of Maxwell's equations in a steep gradient plasma, consideration of the nonequilibrium between electrons and ions, and a model for the electrical and thermal conductivity covering the wide range from the solid state to the high temperature plasma. The simulations are compared with several absorption measurements performed with aluminum targets at normal and oblique incidence. Good agreement is obtained by an appropriate choice of the electron-ion energy exchange time (characterized by 10 to 20 ps in cold solid Al). In addition we discuss the intensity scaling of the temperature, of the pressure, and of the density, where the laser energy is deposited in the expanding plasma, as well as the propagation of the heat wave and the shock wave into the solid. For laser pulse durations $\geqslant 150$ fs considered in this paper the amount of isochorically heated matter at solid density is determined by the depth of the electron heat wave in the whole intensity range.

PACS number(s): 52.50.Jm, 52.40.Nk, 52.65.−y, 52.25.Fi

I. INTRODUCTION

The achievement of ultrashort laser pulses with durations around 100 fs and intensities exceeding 10^{18} W/cm^2 has initiated numerous investigations of laser, interactions with solid matter in a new regime (see, for example, the review article Ref. [1]). In contrast to long nanosecond pulses, ultrashort pulses with a high contrast between the main pulse and prepulse generate a steep gradient plasma with typical scale lengths considerably below the laser wavelength λ. As a consequence, a larger fraction of the laser energy can be coupled to the solid before it expands [2–4]. Recently, isochoric heating of solid aluminum to temperatures of 300 eV has been demonstrated [5]. Thus matter properties like the x-ray opacity [6] or the equation of state can be studied at very high densities. Another important aspect is the study of the electrical conductivity in the transition regime from the solid state to the plasma state [7–10]. As examples for practical applications we mention the generation of ultrashort x-ray pulses [11] to study rapid changes of material properties [12] or material processing on a very fine spatial scale by means of ablation with ultrashort laser pulses [13–15]. At very high intensities the generation of high harmonics with solid targets is also an important issue [16,17].

The coupling of the ultrashort laser pulse to the dense target is a complex process. It involves the absorption of the laser pulse in the steep gradient plasma, whose expansion cannot be neglected unless the intensity is very low or the pulse extremely short, the propagation of an electron heat wave propagating into the solid, and the generation of a shock wave as a consequence of the high pressure. Hydrodynamic codes are a useful tool for a consistent description of these processes provided the laser intensity is not too high. At high laser intensities (S_L) collisionless and relativistic

effects become important. For this situation kinetic simulations are appropriate [18–24]. Recent particle in cell (PIC) simulations including collisions [25] indicate that the validity range of hydrodynamic simulations goes up to $S_L\lambda^2 \approx 10^{17}$ (W/cm^2) μm^2.

In this paper we present a comprehensive study in the regime that can be described by means of a hydrodynamic code. For this purpose we use the one-dimensional hydrodynamic code MULTI [26], which is based on a one-fluid two-temperature model including electronic heat conduction and multigroup radiation transport. For the equation of state (EOS) and the radiative opacities tabulated steady state values are utilized [27,28]. This code had been developed to simulate laser plasma experiments with longer (nanosecond) pulses. In order to cope with the physics of short pulse interaction, the code was modified at three essential points: (1) light propagation in steep gradient matter, (2) modeling of the electron collision frequency, and (3) utilization of separate EOS's for the electrons and the ions.

As to point (1), Maxwell's equations are now solved explicitly on a high resolution mesh, whereas in the original MULTI code a WKB approximation (resulting in Beer's law) was used. Point (2) refers in the first place to the collisional absorption of laser light in the interaction layer, but also to the energy exchange between electrons and ions and to the thermal conductivity which is important for the propagation of the electron heat wave into the dense target. The material state ranges from cold solid to hot ideal plasma, involving quite different physical regimes. Whereas in the plasma regime the electron collision frequency ν is based on Coulomb collisions and thus $\propto T_e^{-3/2}$, ν is determined in the cold solid regime by the interaction between electrons and lattice vibrations (or phonons) and is therefore proportional to the temperature of the heavy particles ($\propto T_i$) [29]. By interpolating

between these two regimes, approximate formulas for the electric conductivity, the electron heat conduction, and the electron-ion relaxation have been introduced. Concerning the last point (3), we used the SESAME EOS [27] calculated separately for electrons and ions instead of only the total EOS as in the original MULTI version [26]. The utilization of a realistic EOS for the electrons including the transition from the degenerate to the nondegenerate state is essential because with ultrashort pulses mainly the electrons are heated.

We would like to emphasize that an important aspect of ultrashort-pulse–target interaction is the strong nonequilibrium between the ions and the electrons. This is because the electron-ion relaxation time, which is in the range of a few tens of ps (Refs. [30–32]), greatly exceeds the duration of the subpicosends laser pulses considered here. Thus the ion temperature is less than the electron temperature by a factor of 10–100. We will discuss this aspect in detail with its consequences on the results. While it has been considered in the analysis of Price *et al.* [10], no detailed results of plasma simulations with nonequilibrium electron and ion temperatures have been presented to date.

The paper is organized as follows. In Sec. II we describe in detail the modifications of the MULTI hydrodynamic code made for ultrashort laser pulses, resulting in the so-called MULTI-FS version. Then, in Sec. III we present results for normal incidence by starting with a comparison with the experiment of Price *et al.* [10]. In detail, we discuss the hydrodynamic behavior such as the importance of the electron-ion relaxation in the lower intensity range, the scaling of the temperature and the pressure with intensity, and the propagation of the heat wave and the shock wave. MULTI-FS is also suitable to simulate oblique incidence. Examples comparing calculations with experiments will be discussed in Sec. IV. Consequences of using steady state EOS and opacity data in the simulation of the short living femtosecond plasma are addressed in the Appendix.

II. THE MULTI-FS HYDRODYNAMIC CODE

In this section we describe the modifications that were made to apply the original long pulse version of MULTI [26] to femtosecond pulses. For completeness the hydrodynamic equations that are solved by MULTI-FS are presented in Appendix A.

A. Solution of Maxwell's equations

For the correct laser energy deposition [$\partial S_L/\partial m$ in Eq. (A3)] in a steep gradient plasma we solved Maxwell's equations by the matrix method described in the textbook of Born and Wolf [33]. To solve the electromagnetic wave equations in an inhomogeneous medium, the profile is subdivided into small slices characterized by the local refractive index $\hat{n} = (\varepsilon)^{1/2}$. For a plasma or a metal with the electron density n_e exposed to a high frequency laser field, $\propto \exp(-i\omega_L t)$, with the frequency ω_L and $\omega_{pe} = (4\pi n_e e^2/m_e)^{1/2}$ (with e and m_e the electron charge and mass, respectively), the complex-valued dielectric constant ε can be written as [33]

$$\varepsilon = \hat{n}^2 = 1 - \frac{\omega_{pe}^2}{\omega_L(\omega_L - i\nu)}, \qquad (1)$$

where ν is the electron collision frequency, which determines the absorption of the laser in the plasma. The validity range of this relation includes the cold metal, provided that no resonances due to interband transitions are present. This condition is fulfilled for aluminum in the optical range, which case is considered in this paper [34].

Since the matrix method requires a very fine grid, we subdivided the Lagrangian grid that is used to solve the hydrodynamic equations. (For the hydrodynamic part of the calculation a less fine grid was taken in order to save computation time.) The values of the temperatures and densities in the finer grid were obtained by a linear interpolation. Tests showed that good accuracy was obtained when the layer thickness of the fine grid (in the nonexpanded solid target) was in the range of 1 Å. The implemented deposition routine allows both normal and oblique incidence with p- or s-polarized laser light.

B. Electrical high frequency conductivity

The refractive index, Eq. (1), contains the electron collision frequency ν. In contrast to long pulses, the laser energy is deposited by femtosocond pulses in a steep gradient plasma at densities ranging from the critical density up to the solid state density; thus ν is needed over a wide temperature and density range including the cold solid and the ideal dilute hot plasma. Since a unique theory for the whole range is not available and more sophisticated models [35–37] are less practicable for code implementation, we apply existing results for the two limiting cases, namely, the cold solid and the hot plasma, and join them smoothly in the transition range. Similar approaches are published in Refs. [38,39].

For the hot plasma we use Spitzer's formula for the collision frequency [40,41]:

$$\nu_{Spitzer} = \frac{4}{3}(2\pi)^{1/2} \frac{Z_{av} e^4 m_e n_e}{(m_e k_B T_e)^{3/2}} \ln(\Lambda). \qquad (2)$$

Here, Z_{av} is the ionization degree, T_e the electron temperature, and $\ln(\Lambda)$ is the Coulomb logarithm, where $\Lambda = [1 + (b_{max}/b_{min})^2]^{1/2}$. The maximum collision parameter is $b_{max} = (k_B T_e/m_e)^{1/2}/\max(\omega_{pe}, \omega_L)$ and the minimum collision parameter $b_{min} = \max[Z_{av} e^2/k_B T_e, \hbar/(m_e k_B T_e)^{1/2}]$. $\hbar$ and k_B are Planck's and Boltzmann's constants, respectively.

In the limit of a cold solid at temperatures below the Fermi temperature (11.7 eV for Al; see Ref. [29]) the electrons are in a degenerate state. The collision frequency is no longer dependent on the electron temperature, but governed by the scattering of electrons by phonons or lattice vibrations [29]. For the corresponding collision frequency we use a formula derived in Ref. [42] for the degenerate matter of white dwarfs or neutron stars. The result is valid at temperatures above the Debye temperature and below the melting point:

$$\nu_{el-phonon} = k_s \frac{e^2}{\hbar v_F}\left(2 - \frac{v_F^2}{c^2}\right)\left[1 + \left(0.13\frac{\hbar\omega_{pi}}{k_B T_i}\right)^2\right]^{-1/2}\frac{k_B T_i}{\hbar}.$$

Here, c is the speed of light, ω_{pi} the ion plasma frequency, and v_F the Fermi velocity [$v_F = \hbar(3\pi^2 n_e)^{1/3}/m_e$]. k_s is a numerical constant, for which the value 13 is given in Ref.
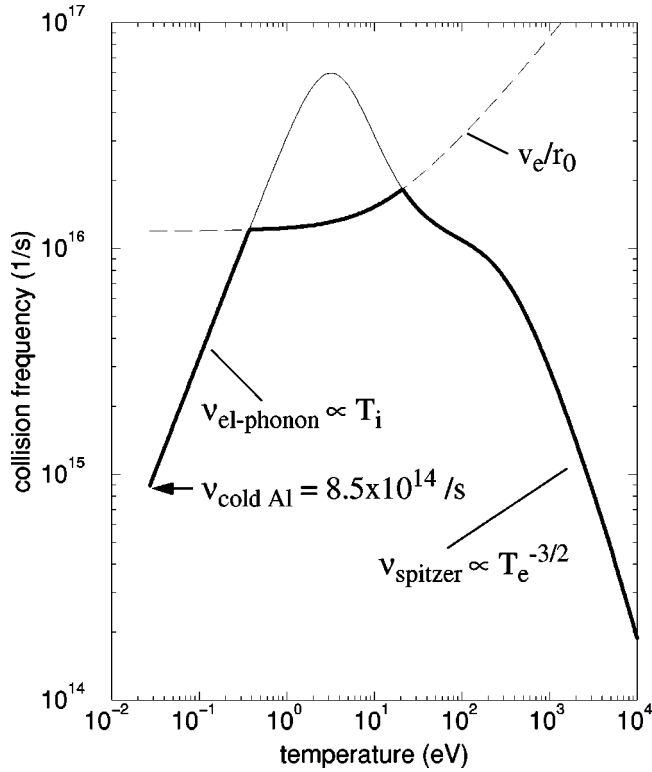
FIG. 1. Collision frequency of solid Al as a function of the temperature $T_e = T_i$ (thick solid line). The thin solid line is the result of the interpolation Eq. (4), the dashed line the upper limit of the collision frequency given by the requirement $\lambda_e > r_0$.

[42]. We use the constant k_s to adapt the collision frequency to measured values of cold metal (see below). For cold solid matter it is $v_F \ll c$ and $\hbar \omega_{pi} \ll k_B T_i$. Thus we have

$$\nu_{el-phonon} \approx 2 k_s \frac{e^2 k_B T_i}{\hbar^2 v_F}. \tag{3}$$

From Eq. (3) follows a linear rise of the collision frequency with the lattice temperature T_i of the solid.

We have interpolated between Eq. (2) and (3) by using the harmonic mean:

$$\nu^{-1} = \nu_{Spitzer}^{-1} + \nu_{el-phonon}^{-1}. \tag{4}$$

Figure 1 illustrates the dependence according to this approximation for solid aluminum ($\rho = 2.7$ g/cm^3) and equal temperatures for the electrons and ions ($T_e = T_i$). Note that this is different from the situation in a femtosecond plasma, where the ions are much colder than the electrons due to the slow electron-ion relaxation (see below). The average ionization Z_{av} in Fig. 1 is calculated by assuming local thermal equilibrium (LTE) and by using the Thomas-Fermi approximation given by More [43]. Figure 1 exhibits the two limiting regimes at high and low temperatures with the scaling $\propto T_e^{-3/2}$ and $\propto T_i$, respectively.

At room temperature the value of ν has been adapted to the value following from the measured reflectivity $R = 0.92$ for Al in the range of visible light. From the relation

$$R = \left| \frac{\hat{n} - 1}{\hat{n} + 1} \right|^2 \tag{5}$$

with $\hat{n}$ given by Eq. (1) one finds $\nu = 8.5 \times 10^{14}$ s^{-1} [assuming an ionization of $Z_{av} = 2.5$ for cold Al (see Ref. [43]) corresponding to a free electron density $n_e = 1.5 \times 10^{23}$ cm^{-3}]. This value of ν (valid for Al) is consistent with the value $k_s = 9.4$ for the numerical constant in Eq. (3).

The maximum value of ν according to Eq. (4) is reached in Fig. 1 at temperatures of a few eV where the aluminum is in a degenerate state. In this range the high [Eq. (2)] and the low [Eq. (3)] temperature approximations are no longer valid: Eq. (2) is invalid because degeneracy and ion correlation effects have to be considered and Eq. (3) is invalid because the temperature exceeds the melting temperature. Examining the electron mean free path λ_e, one finds that around the maximum of ν, λ_e is considerably below the interatomic distance. To avoid this unphysical behavior (the thin solid line in Fig. 1) we use a plausible criterion and require that λ_e should not be smaller than the ion sphere radius r_0:

$$\lambda_e > r_0 = \left(\frac{3}{4 \pi n_i} \right)^{1/3}, \tag{6}$$

where n_i is the ion density. This criterion is equivalent to the requirement

$$\nu < v_e / r_0. \tag{7}$$

As the characteristic electron velocity we use $v_e = (v_F^2 + k_B T_e / m_e)^{1/2}$, which approaches the Fermi velocity in the cold solid and $(k_B T_e / m_e)^{1/2}$ in the hot plasma. This limit is plotted by the dashed line in Fig. 1. Since the electric resistivity is $\propto \nu$, the requirement Eq. (6) or (7) is equivalent to a saturation of the electric resistivity, which has been discussed in Ref. [7]. We note that the utilization of the saturation criterion [Eq. (7)] in the code has no significant effect on the calculated absorption presented below. This is because in the plasma region, where the laser pulse is absorbed, the interatomic distance remains well below the electron mean free path, at least for the cases presented in this paper (see Sec. III C). Thus our results do not critically depend on the exact value of the limitation of the collision frequency.

C. Thermal heat conductivity

The electron collision frequency is also important for the thermal heat conductivity κ, which is related to the electric conductivity (and by that to the collision frequency) via the law of Wiedemann-Franz: $\kappa \propto \sigma T$. In the hot plasma limit Spitzer's result [40] is valid: $\kappa_{Spitzer} = \kappa_0 n_e k_B^2 T_e / (m_e \nu_{Spitzer})$ with $\nu_{Spitzer}$ from Eq. (2). κ_0 is a dimensionless factor, geven by $\kappa_0 = \delta \epsilon 320 / (3 \pi)$. δ and ϵ are correction factors, which are weakly dependent on Z_{av} and tabulated [40]. For fully ionized Al $\kappa_0 = 10$. To extend Spitzer's result to low temperatures we use a similar procedure as in Ref. [38] and replace Spitzer's collision frequency ν_p by the collision frequency ν obtained by the interpolation Eq. (4). This procedure is justified because the heat conductivity of cold degenerate solid metals has, in agreement with

TABLE I. Electron-ion coupling constant g and the characteristic cold ion heating time $\tau_{i,cold} = C_l/g$. The values for Cu, Ag, and Au are taken from Refs. [30–32]. The range indicated for Al is that used in our simulations.

Element	g (W/m^3 K)	C_l (J/g K)	$\tau_{i,cold}$ (ps)
Al	$(1.3-2.6)\times10^{17}$	2.4×10^6	10–20
Cu	10^{17}	3.4×10^6	36
Ag	3.5×10^{16}	2.5×10^6	71
Au	$(2-3.5)\times10^{16}$	2.4×10^6	70–120

the law of Wiedemann-Franz, the same proportionality as the Spitzer conductivity, namely $\kappa_{solid} \propto n_e k_B^2 T_e \tau/m_e$ where $\tau = 1/\nu$ is the electron-ion collision time in the solid [29]. Thus we have

$$\kappa = \kappa_0 \frac{n_e k_B^2 T_e}{m_e \nu}. \qquad (8)$$

According to this approach the temperature scaling is $\kappa \propto T_e^{5/2}$ in the hot plasma and $\kappa \propto T_e/T_i$ in the low temperature regime. Consistency with the cold thermal conductivity is achieved by using an appropriate value for the constant k_s [of Eq. (3)]: For Al Eq. (8) yields with $k_s = 2.3$ (corresponding to a collision frequency $\nu_{el-phonon} = 2.1\times10^{14}$ s^{-1}) the thermal conductivity of solid Al at room temperature $\kappa_{solid} = 2.4$ J (cm s K)$^{-1}$.

D. Electron-ion relaxation

The third important quantity that is related to the electron collision frequency is the electron-ion coupling coefficient γ in Eqs. (A3) and (A4) (see Appendix A). For a hot plasma γ is given by [40]

$$\gamma = \frac{1}{\tau_i}\frac{d\epsilon_i}{dT} = \frac{3m_e k_B \nu}{m_i^2}, \qquad (9)$$

where $d\epsilon_i/dT$ is the specific heat of the ions, which is $3k_B/(2m_i)$ in the ideal gas state. $\tau_i = m_i/(2m_e \nu)$ is the characteristic time for heating the ions. The collision frequency is given by Eq. (2) in the hot plasma ($\nu = \nu_{Spitzer}$).

To cover the whole range of temperatures including the cold solid we generalize Eq. (9) by again using for ν the interpolation formula Eq. (4). To determine the numerical constant k_s in this case we need the electron-ion coupling coefficient for cold solid Al. To our knowledge no measured values have been reported for Al, which is the element that has been used in our simulations. But one can find values for heavier elements in the literature, namely, for Cu [30], Ag [31], and Au [32]. These data have been obtained in pump-probe experiments with ultrashort laser pulses by measuring rapid changes of the reflectivity. In these studies the coupling between the electrons and the cold metal lattice is expressed in terms of $g = \rho\gamma$. The values of g are plotted in Table I along with the values for $\tau_{i,cold} = C_l/g$, where C_l is the heat capacity of the cold metal lattice. As seen from Eq. (A4), the time $\tau_{i,cold}$ describes the heating of the ions during the interaction of the target with the laser pulse [44]. Table I indi-
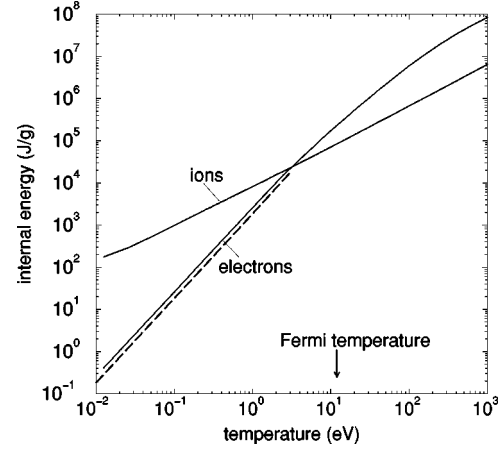

FIG. 2. Specific internal energy of Al as a function of the temperature at $\rho = 2.7$ g/cm^3 for the electrons and ions, respectively. The solid lines are taken from the SESAME library. The dashed line is the electron internal energy of a degenerate free electron gas.

cates that τ_i increases approximately linearly with the mass m_i of the Cu, Ag, and Au atoms. This is expected from the formula $\tau_i = m_i/(2m_e\nu)$, provided that the electron-phonon collision frequency does not depend strongly on the atomic number. Because of the lower mass of the Al atoms, we have therefore tentatively used in our calculations the value $\tau_{i,cold} = 20$ ps (corresponding to $k_s = 13$). It must be noted that the value of $\tau_{i,cold}$ is quite sensitive to absorption at low intensities, because it determines the ion temperature, which in turn determines the collision frequency in the refractive index Eq. (1). To demonstrate this effect we have carried out simulations with different values for the electron-ion coupling in the range given in Table I.

We finally note that $\tau_i \gg \tau_L$ holds in the whole temperature range and we thus expect from Eq. (A4) (see Appendix A) that T_i will always be much smaller than T_e during the laser heating.

E. Equation of state

The separate electron and ion EOS's used in the following simulations are taken from the SESAME library (aluminum, material number 3717, Ref. [27]). The SESAME data for the specific internal energy ($\epsilon_{e,i}$) for the electrons and ions, respectively, at the solid density of Al are plotted in Fig. 2. In the region above the Fermi temperature ϵ_e is given by the sum of the kinetic energy of the electrons $(3/2)n_e k_B T_e/\rho$ and the ionization energy. Below the Fermi temperature the electrons become degenerate and ϵ_e scales $\propto T_e^2$. Thus, with decreasing temperature the internal energy of the electrons drops considerably below that of the ions. For comparison we have also plotted in Fig. 2 ϵ_e of a degenerate free electron gas, which is given by [29]

$$\epsilon_e = \frac{\pi^2}{4}\frac{T_e}{T_F}\frac{k_B T_e n_e}{\rho}. \qquad (10)$$

The values of a free electron gas are slightly below the SESAME values for solid Al. It should be emphasized that for subpicosecond target heating only the electron internal

energy is important, because the ion heating is negligible due to the slow electron-ion energy exchange.

We note that the mean ionization Z_{av} needed for the collision frequency [Eq. (2)] is taken from the SNOP opacity code. For LTE which has been assumed throughout in our simulations this can be considered as a consistent procedure because the ionization resulting for LTE from the SNOP code is very close to the ionization underlying the SESAME data.

III. SIMULATIONS AT NORMAL INCIDENCE

In this section we present simulations performed for normal incidence of the laser. We use the experimental data of Price *et al.* [10] to demonstrate the validity of the model described in the previous section. This experiment was done with 150 fs pulses at $\lambda = 400$ nm emitted by a frequency doubled Ti:sapphire laser. For the laser pulse we applied the time dependence $S_L \propto \sin^2(\pi t/2\tau)$, with τ being the pulse duration (full width at half maximum) . The target material is aluminum. All results presented in this section refer to these irradiation conditions.

Further assumptions (used for all simulations presented in this and the following section) are the following. The target is initially at room temperature $T_e = T_i = 0.0258$ eV and solid Al density $\rho = 2.7$ g/cm^3. It can be considered as a ''massive'' target, i.e., its thickness is large compared to the depth of the region heated by the heat wave or the shock wave. The heat flux inhibition parameter is set to the free streaming limit $f = 0.6$. Its value influences the results only at higher intensities above 10^{16} W/cm^2. The choice of $f = 0.6$ is motivated by recent comparisons of hydrodynamic code calculations with experiments on the heat wave propagation into the solid showing good agreement for $f = 0.6$ [3,45]. The multigroup radiative opacities were calculated with the SNOP code [28] assuming LTE. As discussed in detail at the end of Sec. III C, radiative transport is of minor importance for the conditions of the present study.

A. Laser absorption

Figure 3 compares the calculated absorption with the experiment. The calculated absorption starts at low intensities below 10^{12} W/cm^2 with the value 0.08 corresponding to the reflectivity of cold solid aluminum of 0.92. At intensities above 10^{12} W/cm^2 heating of the ions sets in, which enhances the electron-phonon interaction. Thus the collision frequency and with it the absorption start to rise. At intensities between 10^{14} and 10^{15} W/cm^2 a maximum absorption of about 0.3 is reached. At higher intensities the absorption decreases due to the Coulomb collisions which decrease the collision frequency at the higher temperatures. In this intensity region from 10^{15} to 10^{16} W/cm^2 the calculation somewhat overestimates the measurement. This may be caused by an overestimation of the ionization due to using the LTE approximation, as pointed out in Appendix B. At very high intensities above 10^{17} W/cm^2 the calculation underestimates the experiment. This can be attributed to noncollisional effects which are not taken into account.

For the low intensity range up to the maximum of the absorption, the ion temperature is important for the strength of the electron-phonon interaction, which in turn depends on
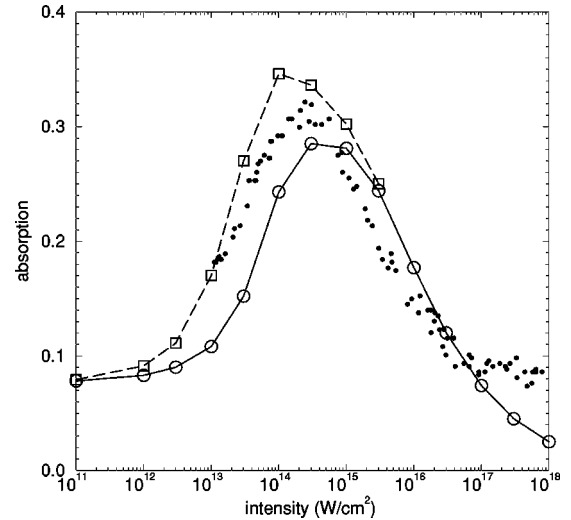

FIG. 3. Absorption as a function of the laser intensity. Pulse duration 150 fs, wavelength 400 nm.The MULTI-FS simulations are done with different electron-ion relaxation times (solid line: $\tau_{i,cold} = 20$ ps, dashed line: $\tau_{i,cold} = 10$ ps). The experimental points are taken from Price *et al.* [10]

the electron-ion energy relaxation. To study this effect we did runs with a changed electron-ion relaxation. In the dashed curve in Fig. 3 our standard value of $\tau_{i,cold} = 20$ ps has been reduced by a factor of 2 ($\tau_{i,cold} = 10$ ps) resulting in enhanced absorption. The experimental data points are in between these two cases, which indicates that the typical cold electron-ion relaxation time is between 10 and 20 ps.

B. Selected simulation at 10^{15} W/cm^2

We will now discuss in detail the hydrodynamic behavior of a selected case, namely, the simulation done at an intensity of 10^{15} W/cm^2, which is close to the maximum absorption of Fig. 3. The laser conditions are the same as in Sec. III A. For the electron-ion energy exchange rate we have used (as well as in Sec. III C) the value $\tau_{i,cold} = 20$ ps.

Figure 4 shows the motion of the Lagrangian cells of the Al target. The mesh has successively finer zoning toward the irradiated side where most of the interaction takes place. Figure 4(a) shows the trajectories of cell interfaces at early times during the interaction with the laser. The front layers expand rapidly with velocities up to a few 10^7 cm/s. As a consequence the laser energy is no longer deposited at solid density. This is seen in Fig. 5 which displays a snapshot at the time of maximum laser intensity $t = 150$ fs of spatial profiles for various quantities. The maximum of the laser energy deposition D occurs at a density (labeled ρ_D in Fig. 5) that is almost 10 times below the solid density. The absorbed energy is mainly found in the thermal energy of the electrons, which are heated up to almost 100 eV. The kinetic energy due to expansion is at this time only a negligible fraction ($\approx 2\%$) of the thermal energy. The spatial profile of T_e extends over a larger range compared to the deposition region, indicating the propagation of a nonlinear heat wave into the solid. The depth of heat wave propagation is given by

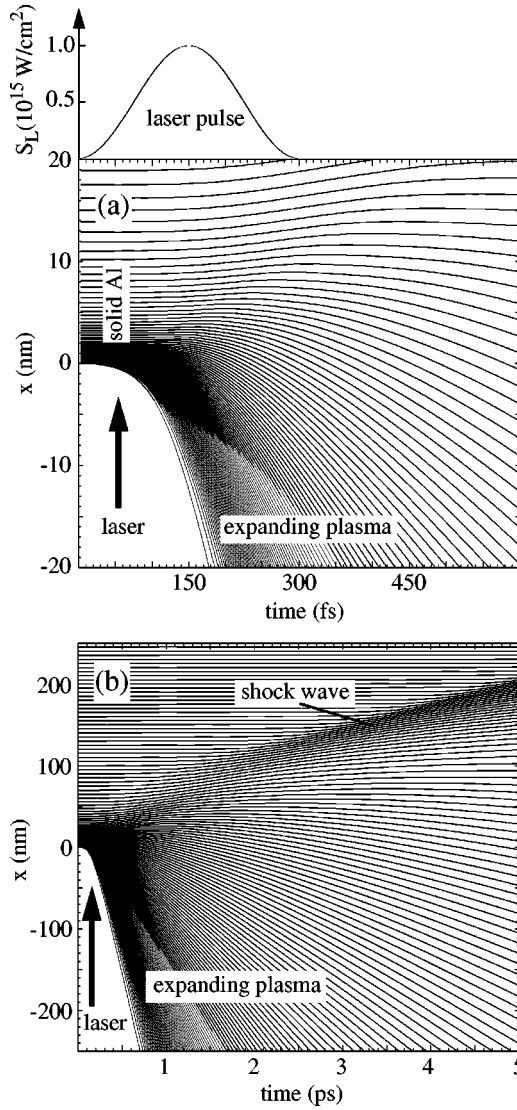$$x_{hw} \approx \sqrt{\chi t}, \chi = \frac{\kappa}{\rho c_p} \propto \lambda_e v_e, \quad (11)$$

FIG. 4. Motion of the Lagrangian cells for a short (a) and a longer time scale (b). Laser conditions as in Fig. 3, $S_L = 10^{15}$ W/cm^2.

where χ is the heat diffusivity and $c_p = d\epsilon_e/dT$ the specific heat of the electrons at constant pressure [46]. This formula yields typical values for x_{hw} of a few tens of nm, as discussed in the next section. The ion temperature is lower than the electron temperature by more than a factor of 10 due to the slow electron-ion relaxation. The peak pressure in the solid reaches 50 Mbar.

After the pulse is switched off, the heat wave propagates further into the solid. But its propagation velocity slows down, because there is no more heating by the laser and the temperature consequently decreases. This is seen in Fig. 6, which shows snapshots of the temperature and density profiles after the laser pulse. The density in the heated range of the solid is initially close to solid density. There is only a little compression caused by the impact of the out-flowing plasma, resulting in an inward motion of deeper layers [Fig. 4(a)]. With time the compression increases and after a few picoseconds a shock wave develops in the solid with a compression ratio exceeding 2, as demonstrated by Figs. 4(b) and 6. This happens at a time t^* when the characteristic length of
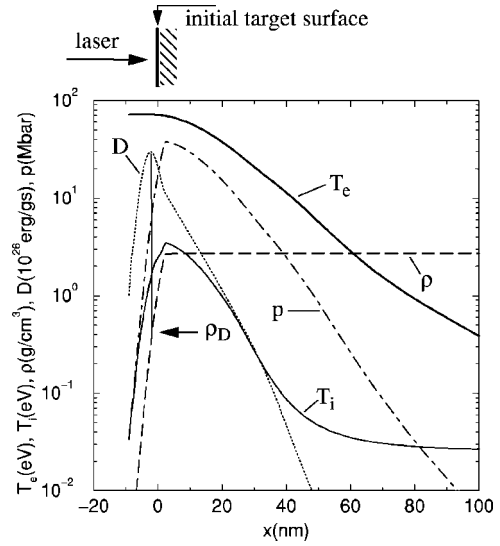

FIG. 5. Spatial dependence of the electron temperature (T_e), the ion temperature (T_i), the mass density (ρ), the pressure (p), and the laser energy deposition (D). Laser conditions as in Fig. 3, $S_L = 10^{15}$ W/cm^2.

hydrodynamic propagation ($x_{hydro} = c_s t^*$, where c_s is the sound velocity) becomes comparable to the depth x_{hw} of heat wave propagation, i.e., at $t^* \approx (1/\nu)(m_i/m_e) \approx \tau_i$. In the dense solid Al heated up to $T_e \approx 10$ eV, electron-ion relaxation times τ_i of a few picosends are expected, which is in agreement with the simulation. This type of shock wave develops under the action of the impulsive load of the expanding target material, as discussed in the book of Zel'dovich and Raizer [46] and in Ref. [47]. In the shock front the ions
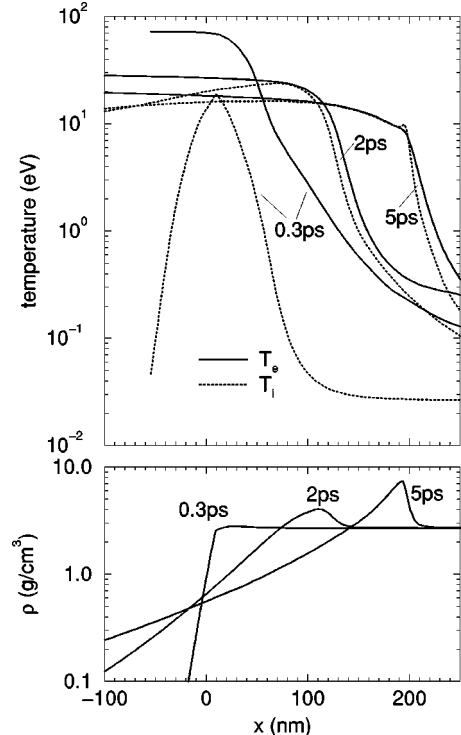

FIG. 6. Temporal development of the spatial distribution of T_e, T_i, and ρ at later times after the interaction with the laser pulse. Laser conditions as in Fig. 3, $S_L = 10^{15}$ W/cm^2.
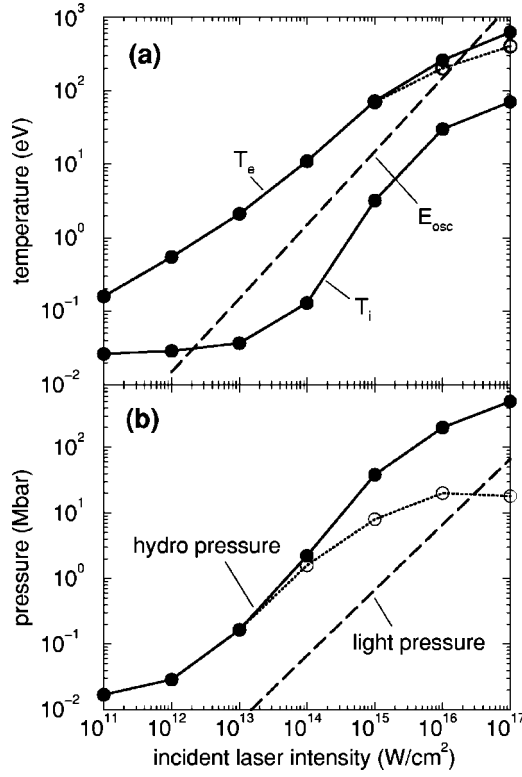
FIG. 7. Intensity dependence of the maximum temperature (a) and the pressure (b). Laser conditions as in Fig. 3 (solid lines). The dotted line in (a) is the electron temperature reached in the solid target (see text). For comparison we plotted also the oscillation energy of the electrons [dashed line in (a)] and the light pressure [dashed line in (b)]. The solid line in (b) is the maximum pressure and the dotted line the pressure in the deposition zone.

are heated, and therefore T_i can exceed T_e as seen in Fig. 6. In front of the shock an electron precursor develops due to the electron heat conduction. Similar shock front structures were observed in Ref. [39].

C. Intensity scaling

In this section we will discuss how the interaction of the laser with the target depends on the laser intensity. Figure 7 shows the dependence of the temperature and the pressure on incident laser intensity S_L. Plotted are the maximum values of T_e, T_i, and p at the time of the pulse maximum ($t = 150$ fs).

Assuming for the intensity scaling of T_e a power law $T_e \propto S_L^\alpha$, the simulation yields $\alpha = 0.5$ for the very low intensity range $S_L \lesssim 10^{13}$ W/cm^2, a faster rise at medium intensities 10^{13} W/cm^2 to 10^{15} W/cm^2 with $\alpha \approx 0.8$, and again a slower increase at the highest intensities $S_L \gtrsim 10^{15}$ W/cm^2. This behavior is the consequence of several effects such as the laser absorption, the depth of the heated target, the scaling of the EOS, and the distribution of absorbed energy over thermal and kinetic energy. The value $\alpha = 0.5$ at very low intensities follows from the $\propto T_e^2$ scaling of the degenerate electron gas [Eq. (10)]. Since the kinetic energy (or expansion) is negligible here, the absorbed energy (per area) $A S_L \tau_L$ is recovered in an increase of the internal energy (per area) $d\rho(\epsilon_e + \epsilon_i)$, where $d\rho$ is the heated mass. Furthermore,

ion heating is negligible and the electrons are in a degenerate state. Thus the specific internal energy is given by Eq. (10) and we find

$$k_B T_e = \sqrt{\frac{4 S_L A \tau_L k_B T_F}{\pi^2 d n_e}} \propto \sqrt{S_L}. \qquad (12)$$

As discussed below, the heated depth is essentially given by heat diffusion rather than the skin depth, i.e., $d \approx x_{hw}$. In the range $S_L \lesssim 10^{13}$ W/cm^2 the values of $A(\approx 0.08)$, x_{hw} (≈ 35 nm), and n_e ($\approx 1.5 \times 10^{23}$ cm^{-3}) do not change significantly; this results in the scaling

$$T_e(\text{eV}) = 0.6 \times \sqrt{S_L/(10^{12} \text{ W/cm}^2)}$$

in good agreement with the temperature plotted in Fig. 7. At higher intensities the situation becomes more complex because the EOS changes from degenerate to nondegenerate including ionization, and because the absorption and the amount of heated mass exhibit a significant dependence on S_L. At very high intensities we have in addition expansion losses (the ratio of kinetic to thermal energy at the end of the laser pulse is 18% at 10^{17} W/cm^2).

The maximum electron temperature plotted in Fig. 7(a) (the full points) is reached at the deposition density ρ_D, which is less than the solid density for $S_L \gtrsim 10^{15}$ W/cm^2. The temperature achieved in the solid target is somewhat smaller as indicated by the open circles in Fig. 7(a). This temperature drop is needed to drive the electron heat flow through the expanding plasma from the deposition region to the solid.

For comparison we also plotted in Fig. 7(a) the energy of the electrons oscillating in the laser field E_L, given by $E_{osc} \propto e^2 E_L^2/(4\omega^2 m_e) \propto S_L$. E_{osc} exceeds T_e at intensities of a few 10^{16} W/cm^2 indicating that above this intensity modifications due to kinetic effects such as anisotropic non-Maxwellian velocity distributions must be expected. We note that according to the Langdon effect [48] deviations from a Maxwellian velocity distribution may occur even at lower intensities, namely, when $Z_{av}E_{osc}$ exceeds $k_B T_e$. The total influence of such kinetic effects is hard to predict: while the Langdon effect would cause a decrease in absorption [48] one expects an increase in absorption from collisionless effects [10].

The ion temperature T_i is considerably below T_e in the whole intensity range due to the slow electron-ion relaxation. At higher intensities $> 10^{15}$ W/cm^2, the ratio T_e/T_i becomes smaller; this is caused by the fact that the maxima of T_i and of T_e do not coincide in space any more: while the maximum of T_e is in the deposition region in the expanding plasma at $\rho_D < \rho_{solid}$, the maximum of T_i is at $\rho = \rho_{solid}$ where the electron-ion collision frequency is high.

The maximum hydrodynamic pressure [Fig. 7(b)] exhibits a similar scaling to the temperature. The maximum pressure is obtained in the solid target, which is efficiently heated by heat conduction. In addition to the maximum hydrodynamic pressure Fig. 7(b) shows also the pressure at the position where the laser energy is deposited. For comparison the light pressure is plotted too. While it is considerably below the maximum hydrodynamic pressure, it exceeds the hydrodynamic pressure in the deposition region at intensities above a
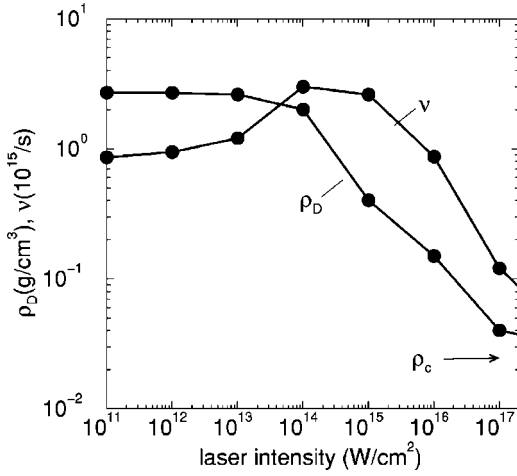
FIG. 8. Intensity dependence of the density ρ_D in the layer of the maximum laser deposition (see Fig. 5) and the collision frequency ν in this layer. Laser conditions as in Fig. 3.

few 10^{16} W/cm^2. Thus modifications caused by the light pressure may occur at these higher intensities. However, since the plasma scale length is in any case small for the short laser pulses considered here (see below), one may expect that profile modifications may become significant at even higher intensities, as has been shown by Peyrusse et al. [49]. (Peyrusse et al. found that significant effects caused by the light pressure require intensities exceeding a few times 10^{17} W/cm^2 and laser pulses longer than 300 fs.)

The deposition density ρ_D (as defined in Sec. III B) is shown in Fig. 8. ρ_D decreases continuously from intensities $>10^{13}$ W/cm^2 and approaches the critical density ρ_c ≈ 0.025 g/cm^3 at $S_L = 10^{17}$ W/cm^2. Figure 8 shows in addition the electron-ion collision frequency calculated for the parameters (n_e, T_e, and T_i) in the deposition region $\rho = \rho_D$ (using $k_s = 9.4$ in the expression for the electric ac conductivity). The dependence $\nu(S_L)$ reflects the absorption dependence in Fig. 3. At intensities between $S_L = 10^{14}$ W/cm^2 and $S_L = 10^{15}$ W/cm^2 where we have maximum absorption, ν reaches maximum values of $\approx 4 \times 10^{15}$ s^{-1}.

It is instructive to consider some characteristic lengths in the plasma and how they depend on intensity. They are shown in Table II. r_0, λ_e, L, and d_s are the ion sphere radius, the electron mean free path, the skin depth, and the plasma scale length, respectively. These quantities refer to the parameters at the maximum of the deposition at $\rho = \rho_D$ at the time of the pulse maximum ($t = 150$ fs). $\lambda_e = (v_F^2 + k_B T_e / m_e)^{1/2}/\nu$ is calculated from the ac conductivity ν (with $k_s = 9.4$). The plasma scale length $L = \rho/\nabla\rho$ is taken directly from density profiles of the simulations. At the highest intensities $S_L > 10^{16}$ W/cm^2, L characterizes also the thickness of the overdense region ranging from $\rho = \rho_D$ to $\rho = \rho_{solid}$, which is two or three times L. The plasma scale length is for all intensities considerably smaller than the laser wavelength $\lambda = 400$ nm. The skin depth follows from the imaginary part of the complex refractive index by the relation [33] $d_s = \lambda/[4\pi \, \text{Im}(\hat{n})]$. The skin depth d_s given in Table II is calculated for a homogeneous plasma with the values for n_e and ν taken at the maximum of the deposition

TABLE II. Characteristic lengths: ion sphere radius r_0, electron mean free path λ_e, plasma scale length L, skin depth d_s, and depth of the electron heat wave x_{hw} for different intensities. r_0, λ_e, d_s, and L refer to the deposition layer, x_{hw} to the solid target. The last two columns give the masses (per area) heated directly by the laser (Δm_D) and by the electron heat flow (Δm_{hw}). Laser conditions as in Fig. 3

S_L (W/cm^2)	r_0 (nm)	λ_e (nm)	L (nm)	d_s (nm)	x_{hw} (nm)	Δm_D (μg/cm^2)	Δm_{hw} (μg/cm^2)
10^{12}	0.158	2.0	≈ 0	7.2	36	2.0	10
10^{13}	0.162	1.6	0.3	7.6	32	2.0	9
10^{14}	0.185	0.7	1.2	9.6	22	1.7	6
10^{15}	0.33	1.7	1.3	11	19	0.7	5
10^{16}	0.42	8	4.5	16	30	0.6	8
10^{17}	0.66	90	13	45	52	0.5	14

D. These values of d_s are approximately equal to the width of the deposition profile, as can be seen, for example, in Fig. 5.

The propagation depth x_{hw} of the heat wave into the solid given in Table II is defined as the length over that the electron temperature decreases by a factor of 2 in the region of the target which has not yet expanded and is still at solid density. Thus x_{hw} characterizes the amount of solid matter that is heated isochorically. The values in Table II are taken from the simulations. They are in good agreement with analytical values obtained by means of Eq. (11). At intensities $\leq 10^{14}$ W/cm^2 the depth of the heat wave x_{hw} is considerably larger than the skin depth d_s. At higher intensities the laser energy deposition no longer occurs in the dense target but in the expanding plasma. Therefore the mass heated directly by the laser is considerably smaller than the dense target mass heated by the electron heat flow. This is illustrated by the last two columns in Table II. $\Delta m_D \approx \rho_D d_s$ is the mass (per area) of the region where the laser energy is deposited (defined by the full width at $1/e$ of the maximum of the deposition D) and $\Delta m_{hw} = \rho_{solid} x_{hw}$ is the mass (per area) heated by the electron flow. The values given in Table II are taken from the simulations. In the whole intensity range Δm_{hw} exceeds Δm_D considerably. The strong decrease of Δm_D at $S_L \geq 10^{15}$ W/cm^2 is a consequence of the scaling of d_s with the density, which is approximately given by $d_s \approx c/\omega_{pe} \propto 1/\sqrt{\rho_D}$; hence $\Delta m_D \approx \rho_D d_s \propto \sqrt{\rho_D}$, i.e., Δm_D becomes smaller with decreasing ρ_D. From these considerations it follows that for the 150 fs pulses considered here the heated depth is essentially controlled by electron heat conduction rather than by the direct laser energy deposition in the skin depth. The situation that the heated depth is determined by the skin depth is expected only for much shorter pulses, when x_{hw} becomes small because of the scaling $\propto \sqrt{t}$ [see Eq. (11)].

Comparing the values for the electron mean free path λ_e and the ion sphere radius r_0 given in Table II, we see that $\lambda_e > r_0$ at all intensities, i.e., the saturation limit $\lambda_e = r_0$ is not reached even at the intensities of highest absorption $S_L = 10^{14} - 10^{15}$ W/cm^2 where λ_e has the smallest value.

The skin depth d_s exceeds the mean free path λ_e at all except the highest intensity 10^{17} W/cm^2. Thus the anomalous skin effect [50] is expected only at $S_L > 10^{16}$ W/cm^2.

At such intensities λ_e also exceeds the plasma scale length L and the depth of the heat wave in the solid, x_{hw}. Consequently our hydrodynamic calculations based on local temperatures may give incorrect results. However, the electron mean free path becomes rapidly smaller when the electrons move toward the solid where the density considerably exceeds the deposition density ρ_D, to which the values of λ_e in Table II refer. (At $S_L = 10^{17}$ W/cm^2 it is $\rho_{solid} \approx 100\rho_D$; thus λ_e is smaller by a factor of ≈ 100 in the region of solid Al.) Therefore it is expected that the electrons will thermalize quickly in the solid and a diffusive heat wave will still exist.

Finally we like to note that MULTI-FS also includes radiative transport and the emission of x rays in the approximation of LTE. Similarly, as observed experimentally (see, for example, Refs. [51,52]), the simulations yield a small amount of emitted x-ray energy E_x compared to the absorbed energy E_{abs}. The ratio E_x/E_{abs} increases from ≈ 0.003 at $S_L = 10^{15}$ W/cm^2 to ≈ 0.03 at $S_L = 10^{17}$ W/cm^2. Thus radiation gives only a small contribution to the energy balance and the energy transport, i.e., it does not influence the hydrodynamic behavior. More accurate values for the x-ray yield may be obtained by using the hydrodynamic results of MULTI-FS for postprocessing, i.e., by solving afterward the rate equations for the populations of the different states of the ions. This was done in Ref. [53], with the result that the LTE approximation may even overestimate the x-ray yield for conditions as considered here.

IV. SIMULATIONS AT OBLIQUE INCIDENCE

As is well known, p-polarized light under oblique incidence considerably enhances the absorption; see, for example, Ref. [54]. To demonstrate the capability of MULTI-FS to describe this situation we have compared the calculations with two experiments.

Figure 9 shows the measurements of Milchberg et al. [7]. These authors measured the reflectivity R of Al under an angle of incidence of 45° as a function of the intensity for s- and p-polarized light. The laser pulse duration was $\tau_L = 400$ fs and the wavelength 308 nm. The simulations start at low intensities with the values for cold solid Al ($A = 5.5\%$ and $A = 10.6\%$ for s- and p-polarization, respectively). The absorption increases with intensity reaching a maximum of nearly 70% for p-polarized light. Again, as in Fig. 3, the simulation results are quite sensitive to the choice of the electron-ion relaxation. The experimental data points are compatible with values of $\tau_{i,cold}$ between 10 and 20 ps.

The other experiment is that of Fedosejevs et al. [8]. In this experiment the reflectivity was measured at a fixed laser intensity ($S_L = 10^{14}$ W/cm^2) as a function of the angle, using 250 fs long laser pulses at a wavelength of 248 nm. In this example also the simulations well describe the experiment (Fig. 10). At large angles the measured points somewhat exceed the calculation, which is in contrast to the cases presented in Figs. 3 and 9. A possible reason may be the depolarization of 7% present in the experiment [8], which diminishes the difference between the values for s and p polarization. Thus, in particular for larger angles, the depolarization causes an overestimation of the measured absorp-
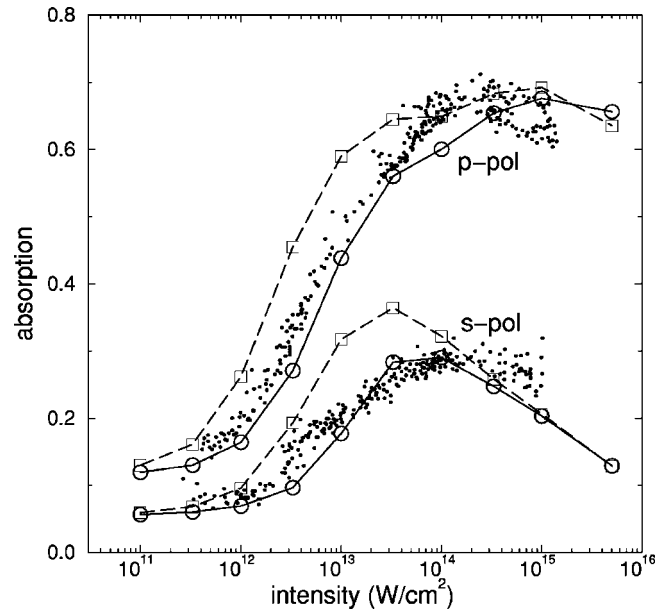

FIG. 9. Absorption at 45° as a function of intensity. Pulse duration 400 fs, wavelength 308 nm. The solid line is calculated with $\tau_{i,cold} = 20$ ps, the dashed line with $\tau_{i,cold} = 10$ ps. The experimental data points (the small dots) are taken from Milchberg et al. [7].

tion for s polarization and an underestimation for p polarization.

We note that we have plotted in Figs. 9 and 10 the absorption $A = 1 - R$ although R was the measured quantity. This is reasonable, because the diffuse scattered light is negligible [10,8]. The absence of diffuse scattering indicates that the reflecting layer is nicely plane, i.e., the one-dimensional plane geometry of the simulations is well matched.

Typical spatial profiles at a fixed time for p-polarized light are shown in Fig. 11 for the conditions of the experiment of Milchberg et al. at the intensity $S_L = 10^{15}$ W/cm^2. At the critical density the deposition peaks strongly, which
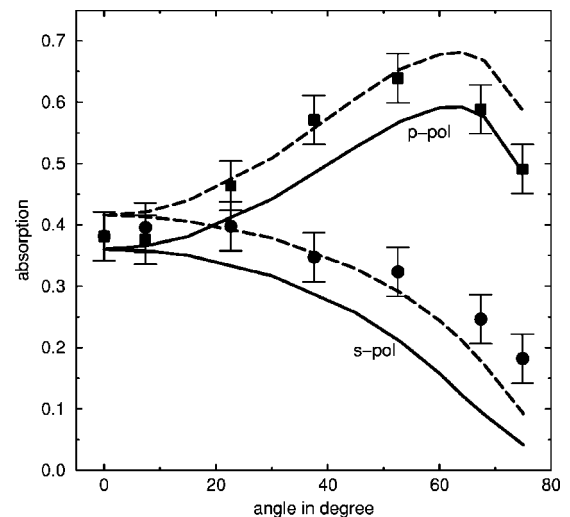

FIG. 10. Absorption as a function of the angle for s- and p- polarized light. The solid line is calculated with $\tau_{i,cold} = 20$ ps, the dashed line with $\tau_{i,cold} = 10$ ps. The experimental data points (the filled circles with experimental error bars) are taken from Fedosejevs et al. [8].
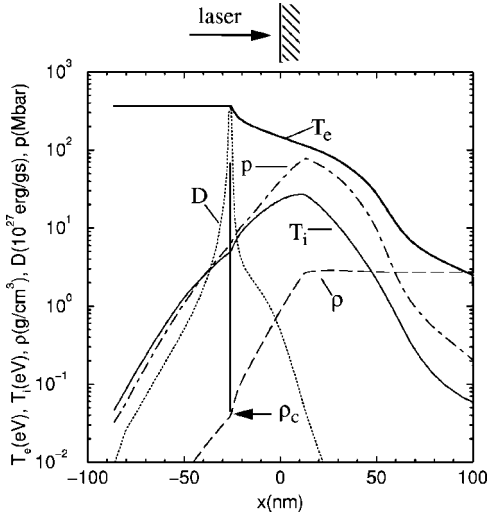
FIG. 11. Snapshot of spatial profiles. p polarization, $S_L = 10^{15}$ W/cm^2, other laser conditions as in Fig. 9.

TABLE III. Characteristic lengths for the conditions of the experiments of Milchberg et al. [7] and of Fedosejevs et al. [8] with p polarization.

Experiment	S_L (W/cm^2)	λ (nm)	L (nm)	x_{osc} (nm)	λ_e (nm)
Milchberg et al.	10^{15}	308	12	0.4	4
Fedosejevs et al.	10^{14}	248	3	0.08	0.25

gives rise to the enhanced absorption. The model using MULTI-FS solves Maxwell's equations with the refraction index Eq. (1). Therefore the absorption peak is caused by a standing plasma oscillation driven by the longitudinal component of the laser field. In reality, plasma waves may be excited. They could cause a wider deposition peak. Nevertheless, the calculated absorption is rather close to the experimental value. This can be attributed to the fact that for resonance absorption the total amount of deposited laser energy is rather independent of the detailed dissipation mechanism [54].

Because the calculated absorption is close to that of the experiment, one can assume that the hydrodynamic quantities are well simulated. Due to the strong deposition at the critical layer the temperature in the expanding plasma is rather high, nearly 400 eV in Fig. 11. There is considerable expansion and the plasma scale length is $L \approx 12$ nm in Fig. 11. Although the deposition occurs in the expanding plasma at the critical layer, there is sufficient heat flow through the expanding plasma for efficiently heating the solid to an electron temperature of 100 eV. For the conditions of the experiment of Fedosejevs et al., the calculated maximum temperature for p polarization at the angle of maximum absorption is ≈ 50 eV and the plasma scale length ≈ 3 nm.

It is of interest to compare the plasma scale length with the amplitude of the oscillating electrons,

$$x_{osc} = \frac{eE}{m_e \omega_L^2} \approx 4.3$$

$$\times (\lambda/(\mu m))^2 (S_L/(10^{15} \ \mathrm{Wcm}^-))^{1/2} \quad \mathrm{nm}.$$

For the experiment of Milchberg et al. one gets at $S_L = 10^{15}$ W/cm^2 and for p polarization $x_{osc} = 0.4$ nm, which is considerably less than the plasma scale length $L = 12$ nm. Thus so-called vacuum heating [18] is negligible under these conditions. For the mean free path of the electrons one finds for the same conditions the value $\lambda_e = 4$ nm. This is three times smaller than L and indicates that electron-ion collisions are important for the absorption process. The different characteristic lengths are summarized in

Table III, which also includes corresponding numbers for the experiment of Fedosejevs et al.

V. SUMMARY AND CONCLUSIONS

We have described the modifications of a nanosecond hydrodynamic code that are necessary to simulate the main physical processes occurring in a plasma created by ultrashort subpicosecond laser pulses. Besides a correct solution of Maxwell's equations in the steep gradient plasma one needs a realistic model for the electrical and thermal conductivity. To cover a large intensity range from 10^{11} to 10^{17} W/cm^2, the transition from the degenerate to the nondegenerate regime must be included. This has been done by joining the low temperature regime with dominating electron-phonon collisions with the high temperature regime characterized by Spitzer's collision frequency. At low temperatures we have adjusted the transport quantities to the measured cold material values. An important point of this paper is the nonequilibrium between the electrons and ions. It requires a two-temperature model for the ions and electrons, taking into account the energy relaxation between the electrons and ions, and separate equations of state for electrons and ions. The model has been applied to aluminum, but it can certainly be used for any metal.

The validity of our model has been tested by comparing measured and calculated absorption. We find good agreement for various experiments at normal and oblique incidence. In the lower intensity range, $S_L \lesssim 10^{15}$ W/cm^2, the ion-electron energy exchange rate is important. Agreement with measurements was obtained by choosing an ion heating time for cold solid Al in the range of 10 to 20 ps, corresponding to a coupling constant $g = (1.3–2.6) \times 10^{17}$ W/m^3 K.

For the laser pulse durations >100 fs considered here, the amount of heated matter is controlled by the depth of the thermal heat wave, which exceeds the skin depth. At higher intensities the laser is absorbed in the expanding plasma, where an ablative heat wave forms. Although the temperature drops in the ablation region, there is still considerable isochoric heating of the solid by the thermal electron heat flow. At the highest intensities 10^{16} to 10^{17} W/cm^2, large energy densities of up to almost 1 Gbar are achievable, which have been confirmed by recent experiments [5,45]. This situation is different from long pulse irradiation where a quasi-steady-state behavior develops and the temperature drops in the ablation region to small values without significant heating of the solid target [55].

Of interest is the question at which intensities the hydrodynamic description with local temperatures is no longer appropriate. The electron mean free path starts to exceed the

typical scale length of the expanding plasma at intensities above 10^{16} W/cm^2. Thus our hydrodynamic model description starts to break down in the absorption region at $S_L \gtrsim 10^{16}$ W/cm^2. However, in the isochorically heated region at solid density the mean free path is still small because of the high density. This is confirmed by recent PIC simulations including collisions [26]. These PIC simulations, performed at intensities of 10^{17} to 10^{18} W/cm^2 at $\lambda = 400$ nm, still show the development of a diffusive heat wave. Its properties are in approximate agreement with hydrodynamic code results. Thus it can be assumed that even under these conditions a diffusive heat wave exists at solid state density. This has also been confirmed by a recent experiment [45].

ACKNOWLEDGMENTS

This work was supported in part by the commission of the European Communities in the framework of the Euratom-IPP association.

APPENDIX A: THE HYDRODYNAMIC EQUATIONS SOLVED BY MULTI-FS

The hydro equations used in this paper differ from the original MULTI version with $T_e = T_i$ of Ramis *et al.* [26] by the consideration of the nonequilibrium between the electron and ion temperatures ($T_e \neq T_i$). In the following we give the complete set of equations solved by MULTI-FS:

$$\frac{\partial v}{\partial t} - \frac{\partial u}{\partial m} = 0, \tag{A1}$$

$$\frac{\partial u}{\partial t} + \frac{\partial (p_e + p_i)}{\partial m} = 0, \tag{A2}$$

$$\frac{\partial \epsilon_e}{\partial t} + p_e \frac{\partial u}{\partial m} = -\frac{\partial S_e}{\partial m} - \sum_k \frac{\partial S_k}{\partial m} + \frac{\partial S_L}{\partial m} - \gamma(T_e - T_i), \tag{A3}$$

$$\frac{\partial \epsilon_i}{\partial t} + p_i \frac{\partial u}{\partial m} = \gamma(T_e - T_i). \tag{A4}$$

$m, v, u, p_{e,i}$, and $\epsilon_{e,i}$ denote the Lagrangian mass coordinate, the fluid velocity, the specific volume ($v = 1/\rho$), the pressure, and the internal energy of the electrons and ions, respectively. $\partial S_e / \partial m$ is the energy deposited by the laser per mass and time. S_e is the electron heat flow. The energy exchange between electrons and ions is described by the coefficient γ, which is discussed in Sec. II D. S_k is the radiative flow of the photon group k with energies $h\nu_k \leq h\nu \leq h\nu_{k+1}$. For details of the radiative transport, which is of minor importance for the femtosecond plasma studied in this paper, we refer to Ref. [26].

APPENDIX B: DEVIATIONS FROM LTE

In the simulations with MULTI-FS we have consistently used the assumption of LTE for the electron EOS and the opacities. We justify this by the necessity to describe the matter over an extremely wide range from the cold solid state to the ideal plasma. In the following we illustrate to
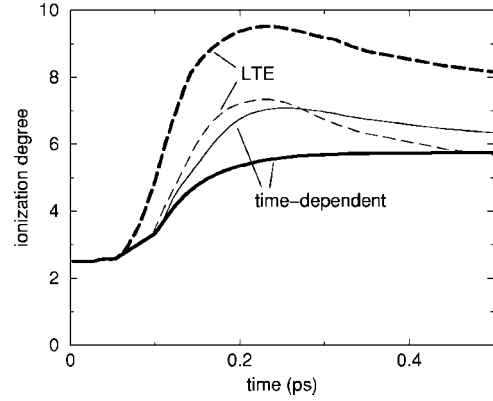

FIG. 12. Mean ionization calculated from rate equations (FLY) compared with the LTE ionization used by MULTI-FS at $S_L = 10^{15}$ W/cm^2 (Laser conditions as in Fig. 3.) The thick lines refer to the layer of maximum laser energy deposition (at the time of the pulse maximum, $t = 150$ fs), the thin lines to a deeper layer in the dense target.

what degree time-dependent effects influence the average ionization and what are the consequences on the absorption.

At higher intensities, when the laser is absorbed in the expanding plasma, the average ionization Z_{av} is overestimated in LTE. This is demonstrated by Fig. 12, where we have plotted Z_{av} for the selected case of Sec. III B in the front layer where the main deposition occurs. We have compared the LTE values by MULTI-FS (calculated with the SNOP code [28]; the thick dashed curve in Fig. 12) with the time-dependent solution, which is obtained by postprocessing the hydrodynamic output of MULTI-FS with the FLY code [56]. This code solves the time-dependent rate equations. The postprocessing method is described in more detail in Ref. [53]. The result obtained in this way by postprocessing is shown by the thick solid curve in Fig. 12, which is significantly below the LTE result. The physical reason for this is that the ionization rate due to electron-ion collisions is not fast enough for the rapidly changing density and temperature. Since the electron-ion collision frequency depends on the ionization degree Z_{av}, the absorption may be overestimated. This could be the reason for the discrepancy in Fig. 3, where in the intensity range 10^{15} to 10^{16} W/cm^2 the calculated absorption is somewhat too high.

To get an idea to what degree the absorption is overestimated, we consider the following arguments. In the selected case under discussion the main deposition occurs at $\rho_D = 0.4$ g/cm^3 at $T_e \approx 70$ eV. Replacing the inhomogeneous spatial profiles of the simulation by a homogeneous plasma with this density and temperature and a sharp vacuum-plasma boundary, we find from Fresnel's formula $A = 0.31$, when we use the LTE ionization for the collision frequency $\nu = 2.6 \times 10^{15}$ s^{-1} [see Eqs. (2) and (4)]. We assume that in a more realistic simulation, which includes the time-dependent effect on Z_{av}, the laser deposition occurs at the same mass density ρ_D and temperature. Then the collision frequency is reduced to the lower value 1.5×10^{15} s^{-1} due to the lower ionization. For the steplike profile we find in this case $A = 0.25$. Thus the overestimation of Z_{av} in LTE may result in an overestimation of the absorption in Fig. 3 by a few percent in the region $S_L \gtrsim 10^{15}$ W/cm^2.

We finally note that the time-dependent solution for Z_{av}

in deeper layers, which are heated isochorically by the electron heat wave, shows only insignificant differences compared to the LTE solution. Thus, this dense region is well described by LTE. This is shown in Fig. 12 by the thin curves for a 4 nm deep layer in the target. We also note that at lower intensities $\leqslant 10^{14}$ W/cm^2, when the deposition occurs at solid density, Z_{av} is well described by LTE for all layers including the front layer where the absorption occurs.

[1] P. Gibbon and E. Förster, Plasma Phys. Controlled Fusion **38**, 769 (1966).

[2] A. Ng, A. Forsman, and P. Celliers, Phys. Rev. E **51**, R5208 (1995).

[3] G. Guethlein, M.E. Foord, and D. Price, Phys. Rev. Lett. **77**, 1055 (1996).

[4] B.K.F. Young, B.G. Wilson, D.F. Price, and R.E. Stewart, Phys. Rev. E **58**, 4929 (1998).

[5] A. Saemann, K. Eidmann, I.E. Golovkin, R.C. Mancini, E. Anderson, E. Förster, and K. Witte, Phys. Rev. Lett. **82**, 4843 (1999).

[6] K. Nazir, S.J. Rose, A. Djaoui, G.J. Tallents, M.G. Holden, P.A. Norreys, P. Fews, P.J. Zhang, and F. Failles, Appl. Phys. Lett. **69**, 3686 (1996)

[7] H.M. Milchberg, R.R. Freeman, S.C. Davey, and R.M. More, Phys. Rev. Lett. **61**, 2364 (1988).

[8] R. Fedosejevs, R. Ottmann, R. Sigel, D. Kühnle, S. Szatmari, and F.P. Schäfer, Phys. Rev. Lett. **64**, 1250 (1990); Appl. Phys. B: Photophys. Laser Chem. **50**, 79 (1990).

[9] A. Ng, P. Celliers, A. Forsman, R.M. More, Y.T. Lee, F. Perrot, M.W.C. Dharma-wardana, and G.A. Rinker, Phys. Rev. Lett. **72**, 3351 (1994).

[10] D.F. Price, R.M. More, R.S. Walling, G. Guethlein, R.L. Shepherd, R.E. Stewart, and W.E. White, Phys. Rev. Lett. **75**, 252 (1995).

[11] J.C. Kieffer, Z. Jiang, A. Ikhlef, and C. Côté, J. Opt. Soc. Am. **13**, 132 (1996)

[12] C. Rischel, A. Rousse, I. Uschmann, P.A. Albouy, J.P. Geindre, P. Audebert, J.C. Gauthier, E. Förster, J.L. Martin, and A. Antonetti, Nature (London) **390**, 490 (1997).

[13] C. Momma, B.N. Chichkov, S. Nolte, F. von Alvensleben, A. Tünnermann, H. Welling, B. Wellegehausen, Opt. Commun. **129**, 134 (1996).

[14] K. Sokolowski-Tinten, J. Bialkowski, A. Cavalleri, D. von der Linde, A. Oparin, J. Meyer-ter-Vehn, and S.I. Anisimov, Phys. Rev. Lett. **81**, 224 (1998).

[15] S.I. Anisimov, N.A. Inogamov, A.M. Oparin, B. Rethfeld, T. Yabe, M. Ogawa, and V.E. Fortov, Appl. Phys. A: Mater. Sci. Process. **69**, 617 (1999).

[16] R. Lichters, J. Meyer-ter-Vehn, and A. Pukhov, Phys. Plasmas **3**, 3425 (1996).

[17] M. Zepf, G.D. Tsakiris, G. Pretzler, I. Watts, D.M. Chambers, P.A. Norreys, U. Andiel, A.E. Dangor, K. Eidmann, C. Gahn, A. Machacek, J.S. Wark, K.J. Witte, Phys. Rev. E **58**, R5253 (1998).

[18] F. Brunel, Phys. Rev. Lett. **59**, 52 (1987).

[19] G. Bonnaud, P. Gibbon, J. Kindel, and E. Williams, Laser Part. Beams **9**, 339 (1991).

[20] P. Gibbon and A. Bell, Phys. Rev. Lett. **68**, 1535 (1992).

[21] S.C. Wilks *et al.*, Phys. Rev. Lett. **69**, 1383 (1992); Phys. Fluids B **5**, 2603 (1993).

[22] H. Ruhl and P. Mulser, Phys. Lett. A **205**, 388 (1995).

[23] T.-Y.B. Yang, W.L. Kruer, A.B. Langdon, and T.W. Johnston, Phys. Plasmas **3**, 2702 (1996); T.-Y.B. Yang, W.L. Kruer, R.M. More, and A.B. Langdon, *ibid.* **2**, 3146 (1995).

[24] A. Pukhov and J. Meyer-ter-Vehn, Phys. Plasmas **5**, 1880 (1998).

[25] R. E. W. Pfund, dissertation, Technische Universität München, 1999.

[26] R. Ramis, R. Schmalz, and J. Meyer-ter-Vehn, Comput. Phys. Commun. **49**, 475 (1988).

[27] S.P. Lyon and J.D. Johnson, Los Alamos National Laboratory Report No. LA-UR-3407, 1992 (unpublished).

[28] K. Eidmann, Laser Part. Beams **12**, 223 (1994).

[29] N. W. Ashcroft and N. D. Mermin, *Solid State Physics* (Saunders College, Philadelphia, 1976).

[30] H.E. Elsayed, T.B. Norris, M.A. Pessot, and G.A. Mourou, Phys. Rev. Lett. **58**, 1212 (1987).

[31] R.H.M. Groeneveld, R. Sprik, and A. Lagendijk, Phys. Rev. Lett. **64**, 784 (1990).

[32] R.W. Schoenlein, W.Z. Lin, J.G. Fujimoto, and G.L. Eesley, Phys. Rev. Lett. **58**, 1680 (1987).

[33] M. Born and E. Wolf, *Principles of Optics* (Pergamon Press, Oxford, 1980).

[34] H. Ehrenreich, H.R. Philipp, and B. Segall, Phys. Rev. **132**, 1918 (1963).

[35] F. Perrot and M.W.C. Dharma-Wardana, Phys. Rev. A **36**, 238 (1987); **163**, 223 (1992).

[36] A.Y. Polishchuk, V.S. Hloponin, and V.E. Fortov, Phys. Lett. A **157**, 406 (1991).

[37] R. Cauble and W. Rozmus, Phys. Rev. E **52**, 2974 (1995).

[38] M. Basko, in *Laser Interaction with Matter and Inertial Fusion*, edited by G. Velarde *et al.* (World Scientific, Singapore, 1997), p. 405.

[39] M. Basko, Th. Löwer, V.N. Kondrashov, A. Kendl, R. Sigel, and J. Meyer-ter-Vehn, Phys. Rev. E **56**, 1019 (1997).

[40] L. Spitzer, Jr., *Physics of Fully Ionized Gases* (Interscience Publishers, New York, 1956).

[41] T.W. Johnston and J.M. Dawson, Phys. Fluids **14**, 722 (1973).

[42] D.G. Yakovlev and V.A. Urpin, Astron. Zh. **57**, 526 (1980) [Sov. Astron. **24**, 303 (1980)].

[43] R. M. More, in *Handbook of Plasma Physics*, edited by M. Rosenbluth, R. Sagdeev, A. Rubenchik, and S. Witkowski (Elsevier, Amsterdam, 1991), Vol. 3.

[44] The ion heating time of the cold lattice should not be confused with the electron cooling time, which is given in Refs. [30–32] as the characteristic equilibration time. This time (≈ 1 ps) is much shorter because of the low heat capacity of a degenerate electron gas compared to the heat capacity of the heavy particles.

[45] A. Saemann, dissertation, Technische Universität Darmstadt, 1998.

[46] Y. B. Zel'dovich and Y. P. Raizer, *Physics of Shock Waves and High-Temperature Hydrodynamic Phenomena* (Academic, New York, 1967).

[47] J. Meyer-ter-Vehn and R. Schmalz, Z. Naturforsch., A: Phys. Sci. **42**, 1096 (1987).

[48] A.B. Langdon, Phys. Rev. Lett. **44**, 575 (1980).

[49] O. Peyrusse, M. Busquet, J.C. Kieffer, Z. Jiang, and C.Y. Côté, Phys. Rev. Lett. **75**, 3862 (1995).

[50] W. Rozmus and V.T. Tikhonchuk, Phys. Rev. A **42**, 7401 (1990)

[51] Z. Jiang, J.C. Kieffer, J.P. Matte, M. Chaker, O. Peyrusse, G. Gilles, G. Korn, A. Maksimchuk, S. Coe, and G. Mourou, Phys. Plasmas **2**, 1702 (1995).

[52] K. Eidmann, A. Saemann, U. Andiel, I.E. Golovkin, R.C. Mancini, E. Anderson, and E. Förster, J. Quant. Spectrosc. Radiat. Transf. **65**, 173 (2000).

[53] K. Eidmann and F. Pisani, in *Laser Interaction with Matter and Inertial Fusion*, edited by G. Velarde *et al.* (World Scientific, Singapore, 1997), p. 465.

[54] W. L. Kruer, *The Physics of Laser Plasma Interactions* (Addison-Wesley, Reading, MA, 1988).

[55] W.M. Mannheimer, D.G. Colombant, and J.H. Gardner, Phys. Fluids **25**, 1644 (1982).

[56] R.W. Lee, B.L. Whitten, and R.E. Strout, J. Quant. Spectrosc. Radiat. Transf. **32**, 91 (1984).